All-Nanosheet Ultrathin Capacitors Assembled Layer-by-Layer *via* Solution-Based Processes

Chengxiang Wang,[†] Minoru Osada,[†] Yasuo Ebina,[†] Bao-Wen Li,[†] Kosho Akatsuka,[†] Katsutoshi Fukuda,[†,‡] Wataru Sugimoto,[‡] Renzhi Ma,[†] and Takayoshi Sasaki[†,*]

[†]International Center for Materials Nanoarchitectonics, National Institute for Materials Science, 1-1 Namiki, Tsukuba, Ibaraki 305-0044, Japan, and [‡]Faculty of Textile Science and Technology, Shinshu University, 3-15-1 Tokida, Ueda, Nagano 386-8567, Japan

ABSTRACT All-nanosheet ultrathin capacitors of $Ru_{0.95}O_2^{0.2-}/Ca_2Nb_3O_{10}^-/Ru_{0.95}O_2^{0.2-}$ were successfully assembled through facile room-temperature solution-based processes. As a bottom electrode, conductive $Ru_{0.95}O_2^{0.2-}$ nanosheets were first assembled on a quartz glass substrate through a sequential adsorption process with polycations. On top of the $Ru_{0.95}O_2^{0.2-}$ nanosheet film, $Ca_2Nb_3O_{10}^-$ nanosheets were deposited by the Langmuir–Blodgett technique to serve as a dielectric layer. Deposition parameters were optimized for each process to construct a densely packed multilayer structure. The multilayer buildup process was monitored by various characterizations such as atomic force microscopy (AFM), ultraviolet–visible absorption spectra, and X-ray diffraction data, which provided compelling evidence for regular growth of $Ru_{0.95}O_2^{0.2-}$ and $Ca_2Nb_3O_{10}^-$ nanosheet films with the designed multilayer structures. Finally, an array of circular films (50 μm ϕ) of $Ru_{0.95}O_2^{0.2-}$ nanosheets was fabricated as top electrodes on the as-deposited nanosheet films by combining the standard photolithography and sequential adsorption processes. Microscopic observations by AFM and cross-sectional transmission electron microscopy, as well as nanoscopic elemental analysis, visualized the sandwich metal–insulator–metal structure of $Ru_{0.95}O_2^{0.2-}/Ca_2Nb_3O_{10}^-/Ru_{0.95}O_2^{0.2-}$ with a total thickness less than 30 nm. Electrical measurements indicate that the system really works as an ultrathin capacitor, achieving a capacitance density of ~27.5 μF cm^{-2}, which is far superior to currently available commercial capacitor devices. This work demonstrates the great potential of functional oxide nanosheets as components for nanoelectronics, thus contributing to the development of next-generation high-performance electronic devices.

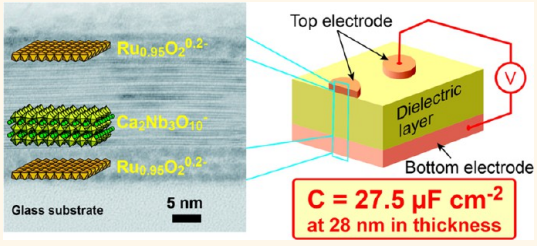

KEYWORDS: oxide nanosheets · ultrathin capacitors · solution-based assembly processes · dielectric property · capacitance density

The capacitor is a widely used electric storage device indispensable in electric and electronic applications. Because capacitors are the largest elements in current electronic devices, increasing their capacitance in smaller areas/volumes is an important step in the advancement of electronics.[1,2] Significant downsizing of capacitors has been successfully accomplished through improvements in various factors, *e.g.*, adoption of high dielectric constant (high-*k*) materials, thinning of the dielectric layer, and multilayer implementation of metal–insulator–metal (MIM) units. However, this technology has almost reached saturation in both materials and processing, making it difficult to achieve further performance upgrades.

For example, in multilayer ceramic capacitors (MLCCs), indispensable electronic components for advanced electronic technology, relentless advances in microelectronic packaging, and communication technologies require the miniaturization and integration of the MLCCs.[3−5] Barium titanate ($BaTiO_3$: BT) is one of the most important dielectric materials widely used for MLCCs. The continuing demand to further miniaturize MLCCs has led to the downsizing of BT ceramics to a nanometer scale. State-of-the-art technology enables the fabrication of the multilayer structure with a thin BT ceramic layer of around 0.5 μm using ~100 nm size BT particles, and the commercialization of the smallest size MLCCs (0.4 × 0.2 mm^2) has recently been realized by Murata Manufacturing Co.[6] Keen demand for continuing miniaturization of MLCCs requires the fabrication of thinner dielectric layers, but this presents more

* Address correspondence to sasaki.takayoshi@nims.go.jp.

Received for review December 12, 2013 and accepted February 3, 2014.

Published online February 03, 2014
10.1021/nn406367p

significant issues. As the size of BT particles decreases to below 100 nm, the formidable challenge lies in a gradual decline in the dielectricity (the so-called size effect), which impedes the progress of MLCC technology. Thus, a novel solution has been eagerly anticipated in this field.

Such materials and processing issues are clearly exposed also in thin-film-based nanocapacitors. The nanocapacitors based on $SrTiO_3$ and $(Ba,Sr)TiO_3$ yield reduced relative permittivity (ε_r) values that are a few orders of magnitude smaller than bulk ones. The situation is even more complicated in actual systems. Due to their rather complex compositional and structural aspects, uniformity and homogeneity of composition and crystal structure, crucial to high-*k* dielectric thin layers, are difficult to control over a large area by current methods[7−11] such as CVD,[12,13] ALD,[14−17] MOCVD,[18−20] and the sol−gel process.[21] Furthermore, these techniques generally require high-temperature and elaborate deposition processes, often producing undesirable interface reactions and/or thermal strain between the high-*k* layers and electrodes. This so-called "dead-layer" problem results in greatly degraded ε_r of the sensitive high-*k* thin films.[22−24]

As a means of overcoming these issues in current capacitors, nanocrystal technology is an emerging research area, with the goal of using nanomaterials as core device components. A unique strategy involving layer-by-layer deposition of metal oxide nanosheets has opened up a novel route for this challenge. The oxide nanosheets derived from a precursor layered compound *via* exfoliation are molecularly thin two-dimensional (2D) crystals, holding a fixed stoichiometric composition and a 2D crystalline lattice inherited from the parent compounds. They have a material-dependent unique thickness of 0.5−3 nm. On the other hand, the lateral dimension is typically in a micrometer range, primarily determined by the size of the starting layered compound and mechanical shear applied in the delamination process. We have reported the synthesis of a range of oxide nanosheets including dielectric nanosheets, such as $Ti_{0.87}O_2^{0.52-}$,[25] $Ca_2Nb_3O_{10}^-$,[26] $Ti_2NbO_7^-$,[27] and metallic conductive $Ru_{0.95}O_2^{0.2-}$ nanosheets.[28,29] Among various dielectric oxide nanosheets, perovskite-type $Ca_2Nb_3O_{10}^-$ nanosheets exhibit a remarkably high permittivity of $\varepsilon_r >$ 200 even in the ultrathin region (5−20 nm), which is more than 10 times larger than that of $(Ba_{1-x}Sr_x)TiO_3$ films at the same thickness.[30] The high ε_r value remains virtually constant (size-effect free). These features indicate that this nanosheet can be an effective dielectric component in high-density and ultrathin capacitor applications. Moreover, high electrical conductivity of $Ru_{0.95}O_2^{0.2-}$ nanosheets has been demonstrated,[28] suggesting that it has promising potential as an ideal building block in constructing electrodes of ultrathin capacitors.

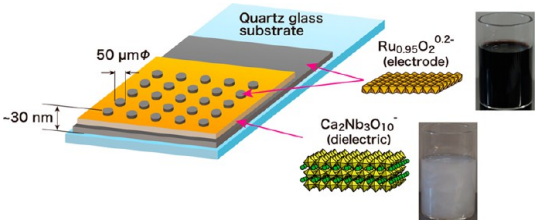

Figure 1. Schematic illustration of the all-nanosheet ultrathin capacitor of $Ru_{0.95}O_2^{0.2-}/Ca_2Nb_3O_{10}^-/Ru_{0.95}O_2^{0.2-}$.

These oxide nanosheets can be assembled *via* room-temperature solution-based processes into ultrathin films, which is another important advantage. On the basis of their polyanionic colloidal nature, a sequential adsorption process and the Langmuir−Blodgett (LB) technique can be applied to deposit them layer-by-layer into precisely organized lamellar nanostructures. We have fabricated multilayer films of $Ca_2Nb_3O_{10}^-$ nanosheets on a $SrRuO_3$ single-crystal substrate *via* this process and then deposited Au top electrodes by a conventional sputtering technique to construct a MIM device, which was proved to work as a capacitor with superior high-*k* performance.[26,30,31]

Considering these promising aspects, the sequential organization of $Ru_{0.95}O_2^{0.2-}$ and $Ca_2Nb_3O_{10}^-$ nanosheet films into a sandwich structure would be a powerful approach to construct high-performance ultrathin capacitors. Manufacturing such a MIM device by solution-based processes throughout without employing a vacuum-based technique is important from a practical viewpoint. Furthermore, interface reaction between the dielectric layer and the electrodes, which is fatally harmful to the performance of ultrathin capacitors, is expected to be suppressed *via* this approach involving soft-chemical processes, which can be conducted under mild conditions. Well-defined stoichiometric composition and highly crystalline 2D structure of nanosheets will guarantee the compositional and structural uniformity across such nanosheet films. An ideal interface matching between $Ru_{0.95}O_2^{0.2-}$ and $Ca_2Nb_3O_{10}^-$ nanosheets, which is also important for the performance of capacitors, would be attained thanks to the intrinsic angstrom-level flatness of the nanosheets. In addition, other techniques such as photolithography can be incorporated to achieve patterning of the nanosheet films. It is therefore expected that this strategy has great potential for building high-performance ultrathin capacitors.

RESULTS AND DISCUSSION

Designed Structure of All-Nanosheet Capacitors. Figure 1 illustrates the schematic MIM structure of $Ru_{0.95}O_2^{0.2-}/Ca_2Nb_3O_{10}^-/Ru_{0.95}O_2^{0.2-}$ designed as the all-nanosheet ultrathin capacitor on quartz glass substrates. A multilayer film of $Ru_{0.95}O_2^{0.2-}$ nanosheets was employed as a bottom electrode. A previous study reported that the film had a substantially high electrical conductivity

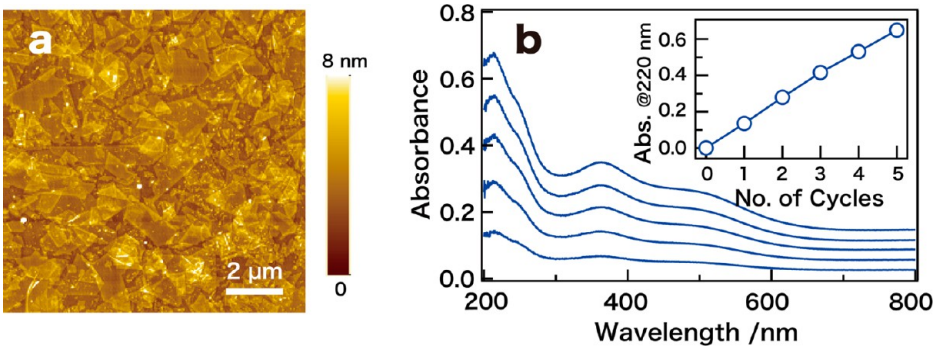

Figure 2. (a) AFM image of a monolayer film of $Ru_{0.95}O_2^{0.2-}$ nanosheets on a Si substrate. (b) UV−visible absorption spectra of $Ru_{0.95}O_2^{0.2-}$ nanosheet films deposited on both sides of a quartz glass substrate from one to five layers. The inset shows the absorbance at 220 nm as a function of cycle numbers.

(~1 kΩ sq^{-1}), which was compatible with use as an electrode.[28] The conductivity was found to be enhanced as the layer number of $Ru_{0.95}O_2^{0.2-}$ nanosheets increased, which was accounted for by the development of lateral conduction paths *via* percolation. On the other hand, a thicker film tends to be rougher on the surface, which will prevent the deposition of a well-organized film of dielectric nanosheets on top of the $Ru_{0.95}O_2^{0.2-}$ nanosheet film. It is known that a high film quality, *e.g.*, highly dense and lamellar packing of the nanosheets, is crucially important to fully attain the superior dielectric performance inherent to the oxide nanosheets.[25,30] Such film quality is sensitively dependent on the roughness of the substrates. As a compromise in the pursuit of these two contradictory factors, we selected a two- to five-layer film of $Ru_{0.95}O_2^{0.2-}$ nanosheets as the underlying bottom electrodes. The dielectric layer is composed of a ten-layer $Ca_2Nb_3O_{10}^-$ nanosheet film, for which high dielectric and insulating performance has been demonstrated. For the top electrode, the multilayer film of $Ru_{0.95}O_2^{0.2-}$ nanosheets was also employed, but it was fabricated into an array of circular films with a diameter of 50 μm ϕ for the convenience of electrical property measurements.

Fabrication of Multilayer Films of $Ru_{0.95}O_2^{0.2-}$ Nanosheets as a Bottom Electrode. $Ru_{0.95}O_2^{0.2-}$ nanosheets were sequentially adsorbed with polycationic copolymer on Si and quartz glass substrates. Figure 2a depicts the surface topography for a monolayer film of the nanosheets deposited on a Si substrate under optimized conditions. A similar high-quality film could also be fabricated on a quartz glass plate. The substrate surface is densely covered with $Ru_{0.95}O_2^{0.2-}$ nanosheets with a thickness of ~1.1 nm (Figure S1a and S1b). The height histogram analysis revealed a high surface coverage of >90% with an overlapped portion of <10%. A previous study reported that a coverage of >70% can yield good electrical conductivity, developing substantial conduction paths *via* percolation through bridges of overlapped nanosheets.[28] Thus the attained surface coverage of >90% (Figure 2a) is considered to be high enough. In practice, we repeated the deposition leading to two- and five-layer films to enhance the conductivity and mechanical strength (Figure S1c and S1d). The deposition process can be conveniently monitored by UV−visible absorption spectra. The $Ru_{0.95}O_2^{0.2-}$ nanosheets show optical absorption in a wide wavelength range associated with its metallic nature. The absorbance was progressively enhanced with the number of deposition cycles, indicating the regular repetition of the above-mentioned deposition of nanosheets to produce a multilayer nanostructured film.

The films were masked and coated with Au electrodes in order to measure the sheet resistance. The two-layer and five-layer films on quartz glass substrates afforded a highly conducting nature with room-temperature sheet resistances of ~4.1 and ~0.9 kΩ sq^{-1}, respectively, in accordance with the previous study.[28] The films were flat enough to serve as the bottom electrodes. The surface roughness (R_a) was ~1.0 and ~1.4 nm for the two-layer and five-layer films, respectively, as revealed by AFM analysis. This flat surface attained can be ascribed to the 2D anisotropic structure of the nanosheets with atomically flat terraces. We note that resistances of our films are comparable to those of rutile RuO_2 thin films epitaxially grown by a sophisticated vacuum-deposition technique. RuO_2 is agreed to be the most promising electrode material for high-*k* materials thanks to its high conductivity, high thermal stability, and high work function.[32−35] The flat and highly conducting nature of $Ru_{0.95}O_2^{0.2-}$ nanosheet films, which compares favorably with epitaxial RuO_2 thin films, ensures that they can serve as the bottom electrodes for the LB deposition of $Ca_2Nb_3O_{10}^-$ nanosheet films in the next step.

Deposition of Multilayer Films of $Ca_2Nb_3O_{10}^-$ Nanosheets as a Dielectric Layer. The dielectric layers of high-*k* $Ca_2Nb_3O_{10}^-$ nanosheets were sequentially deposited on top of the as-prepared $Ru_{0.95}O_2^{0.2-}$ bottom electrodes by means of the LB process, which was effective in building up high-quality nanosheet films. The $Ca_2Nb_3O_{10}^-$ nanosheets are ~1.4 nm in thickness and 2−6 μm in lateral size (Figure S2). The large lateral size is favorable to the production of a highly insulating film without substantial

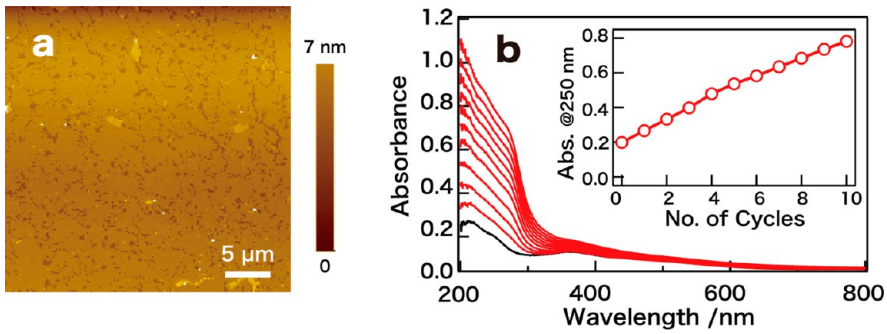

Figure 3. (a) AFM image of a monolayer film of $Ca_2Nb_3O_{10}^-$ nanosheets on a Si substrate. (b) UV−visible absorption spectra of multilayer films of $Ca_2Nb_3O_{10}^-$ nanosheets (red lines) on a two-layer film of $Ru_{0.95}O_2^{0.2-}$ nanosheets (black line). The inset shows the absorbance at 250 nm as a function of cycle numbers.

leakage paths. When the suspension of $Ca_2Nb_3O_{10}^-$ nanosheets was placed in the LB trough, nanosheets floated at the air/water interface due to the moderate amphiphilic role of tetrabutylammonium (TBA) ions, which were used as a delaminating agent.[36] Then they were gathered and packed together by moving two barriers inward and subsequently transferred onto the substrate surface by a lifting-up process. With optimized deposition parameters, a monolayer film of neatly tiled $Ca_2Nb_3O_{10}^-$ nanosheets was produced through this process. A fairly uniform and homogeneous texture, *i.e.*, atomically flat film (R_a ~0.3 nm) was attained across the substrate surface (Figure 3a). This LB transfer was repeated 10 times to produce a ten-layer nanosheet film. AFM images shown in Figure S3 indicate that the obtained ten-layer films are still flat. UV−visible absorption spectra monitoring the deposition process show the progressive enhancement of absorption due to the $Ca_2Nb_3O_{10}^-$ nanosheets, which was superimposed onto the features derived from the $Ru_{0.95}O_2^{0.2-}$ nanosheet film. The nearly linear increment in absorbance (inset of Figure 3b) indicates the successful layer-by-layer deposition of $Ca_2Nb_3O_{10}^-$ nanosheets. The nanosheets were assembled into a multilayer film accommodating TBA ions in their galleries. Note that TBA ions are decomposed into small inorganic cations such as H^+ and NH_4^+ *via* the photocatalytic action of the $Ca_2Nb_3O_{10}^-$ nanosheet activated by UV illumination during the deposition process.[37]

Figure 4 depicts X-ray diffraction (XRD) data of the fabricated films of $(Ru_{0.95}O_2^{0.2-})_n/(Ca_2Nb_3O_{10}^-)_{10}$ (n = 2, 5). Control data for a film directly deposited on the quartz glass substrate without the prime coat layer of $Ru_{0.95}O_2^{0.2-}$ nanosheets showed five peaks at 5.48°, 11.05°, 22.33°, 40.18°, and 45.85° in 2θ, which are attributable to 001, 002, 004, 007, and 008 reflections, respectively, from the multilayer structure of $(Ca_2Nb_3O_{10}^-)_{10}$. The multilayer spacing of 1.6−1.7 nm is comparable to those obtained in our previous study for the film on an atomically flat $SrRuO_3$ substrate. Observation of the higher-order basal peaks suggests a well-organized lamellar structure composed of stacked nanosheets. The XRD pattern for the sample with a two-layer film of $Ru_{0.95}O_2^{0.2-}$

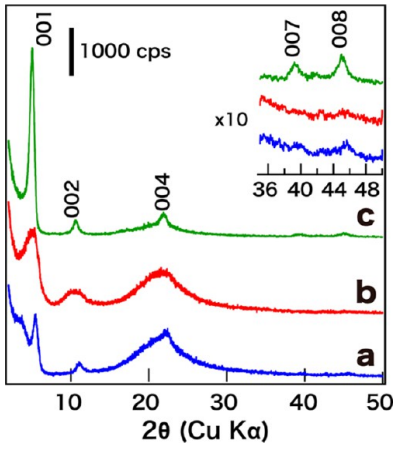

Figure 4. XRD patterns of nanosheet films of $(Ca_2Nb_3O_{10}^-)_{10}$ fabricated on a quartz glass substrate covered with a (a) two- and (b) five-layer film of $Ru_{0.95}O_2^{0.2-}$ nanosheets, respectively. Trace (c) is control data from a bare quartz glass substrate. A broad hump at 15−30° in 2θ is due to the amorphous halo from the quartz glass substrate. The inset corresponds to 10-fold patterns of (a), (b), and (c) between 35° and 50°.

nanosheets was similar to that for the control data except for the lower intensity of the peaks. As a result, a halo hump from the glass substrate was relatively noticeable. However, 004, 007, and 008 peaks were still barely detectable. These weak reflections may be due to the fact that the film was deposited onto the underlying $Ru_{0.95}O_2^{0.2-}$ nanosheet films, which inevitably had a larger surface roughness. This effect became further enhanced for the sample with a five-layer film of $Ru_{0.95}O_2^{0.2-}$ nanosheets. The 001 and 002 peaks broadened significantly, and the other peaks were nearly unobservable. On the other hand, diffraction features from $Ru_{0.95}O_2^{0.2-}$ nanosheet films were not clearly detected. The limited number of stacked layers of rather flexible $Ru_{0.95}O_2^{0.2-}$ nanosheets may be responsible for this absence.

Fabrication of Patterned Films of $Ru_{0.95}O_2^{0.2-}$ Nanosheets as a Top Electrode. We have developed the following procedures to design an array of circular electrodes composed of $Ru_{0.95}O_2^{0.2-}$ nanosheets. As illustrated in Figure 5, the process involves photolithography

combined with the deposition technique *via* sequential adsorption (for details, refer to Materials and Methods). The feasibility of the process was first demonstrated on a bare Si substrate. The substrate was completely covered with the photoresist by a spin-coating process. Then the hollow columnar patterns were formed on the resist layer *via* photolithography and developing processes. In the following step, $Ru_{0.95}O_2^{0.2-}$ nanosheets were deposited layer-by-layer, typically two and five times, into the hollow columns *via* sequential adsorption with copolymer. After removing the photoresist layer in the final step, a well-organized array of the circular films of $Ru_{0.95}O_2^{0.2-}$ nanosheets appeared as depicted in Figure 6. Circular nanosheet films with a diameter of 50 μm were regularly arranged to form a square lattice pattern with a repeating distance of 250 μm, thus substantiating the feasibility of such a combination.

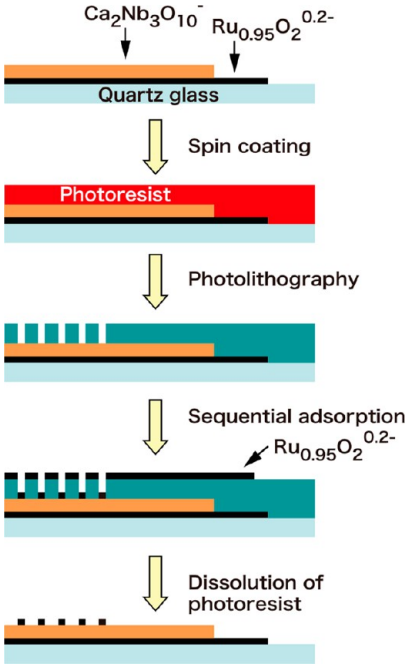

Figure 5. Schematic diagram for the fabrication process of an array pattern of circular films of $Ru_{0.95}O_2^{0.2-}$ nanosheets. Step 1: As-prepared nanosheet film of $Ru_{0.95}O_2^{0.2-}$/$Ca_2Nb_3O_{10}^-$. Step 2: Complete coverage of the film surface with photoresist by spin-coating. Step 3: Formation of hollow columnar patterns onto the photoresist layer *via* photolithography and a developing process. Step 4: Deposition of $Ru_{0.95}O_2^{0.2-}$ nanosheets by a sequential adsorption process. Step 5: Removal of the photoresist layer.

Prior to application of this technique to the designed film of $(Ru_{0.95}O_2^{0.2-})_n/(Ca_2Nb_3O_{10}^-)_{10}$ (n = 2, 5), an assessment was made about whether the photolithography process would damage the nanosheet films. UV–visible absorption spectra were used to monitor possible changes in the nanosheet films, for example, peeling off or chemical modification, by utilizing its high sensitivity to the nanosheet. There was almost no detectable difference in absorbance from the nanosheet films after the treatments (Figure S4), indicating that $Ca_2Nb_3O_{10}^-$ and $Ru_{0.95}O_2^{0.2-}$ nanosheet films remained intact during the process. Then all-nanosheet MIM assemblies were completed by depositing the patterned circular films (50 μm ϕ) of $Ru_{0.95}O_2^{0.2-}$ nanosheets on top of the film of $(Ru_{0.95}O_2^{0.2-})_n/(Ca_2Nb_3O_{10}^-)_{10}$.

Characterization of the Fabricated MIM Structure. The all-nanosheet MIM devices constructed on quartz glass substrates (12 × 50 mm^2) were visibly transparent, as shown in a typical example of $(Ru_{0.95}O_2^{0.2-})_5/(Ca_2Nb_3O_{10}^-)_{10}/(Ru_{0.95}O_2^{0.2-})_5$ in Figure 7a. This can be ascribed to the ultrathin thickness and weak or negligible absorption of $Ru_{0.95}O_2^{0.2-}$ and $Ca_2Nb_3O_{10}^-$ nanosheets in the visible light range. Observations by scanning electron microscopy (SEM) and optical microscopy clearly indicate that the circular films of $Ru_{0.95}O_2^{0.2-}$ nanosheets were deposited on the surface as designed (Figure 7b and Figure S5). More detailed morphology of the circular film was visualized by AFM analysis, which gave its height as ~6 nm (Figure 7c). This value is compatible with a thickness of five-layer stacks of $Ru_{0.95}O_2^{0.2-}$ nanosheets. Note that the thickness of the monolayer $Ru_{0.95}O_2^{0.2-}$ nanosheets was estimated as ~1.1 nm (Figure S1). Cross-sectional high-resolution transmission electron microscopy (HRTEM) provides direct information about the nanoscopic

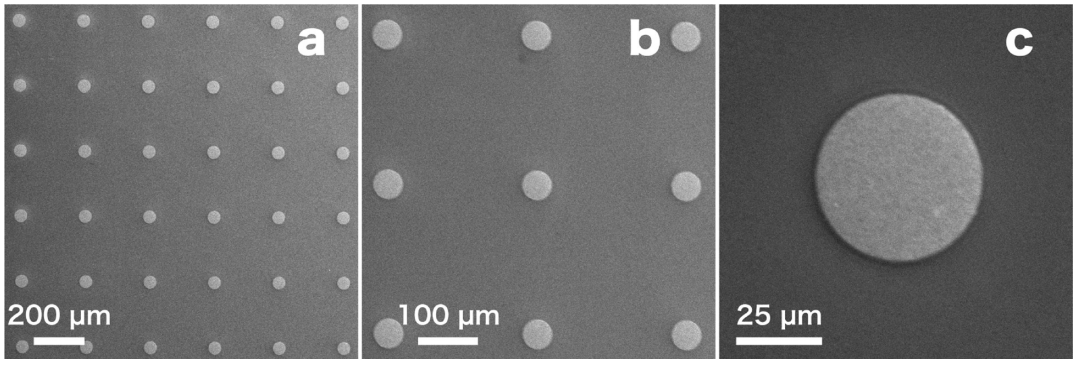

Figure 6. SEM images of an array pattern of circular films of $Ru_{0.95}O_2^{0.2-}$ nanosheets fabricated on the Si substrate by photolithography and sequential adsorption processes. The diameter of the circles is 50 μm.

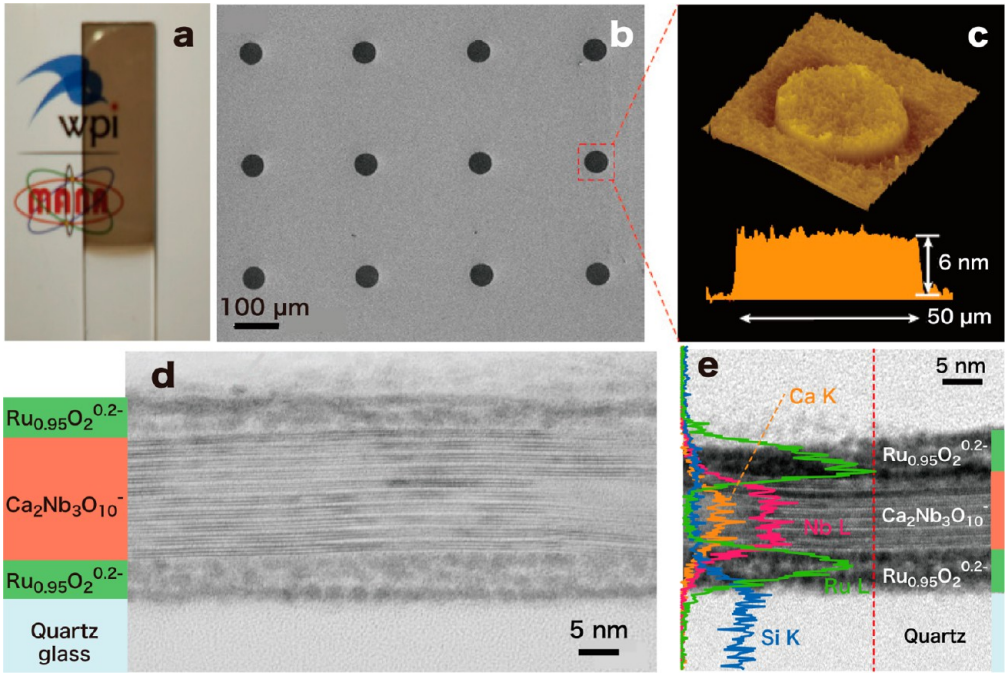

Figure 7. (a) Photograph of the all-nanosheet capacitor of $(Ru_{0.95}O_2^{0.2-})_5/(Ca_2Nb_3O_{10}^-)_{10}/(Ru_{0.95}O_2^{0.2-})_5$ fabricated on a quartz substrate. (b) SEM image of an array of circular films of $Ru_{0.95}O_2^{0.2-}$ nanosheets on the surface. (c) Three-dimensional AFM image of a top electrode of $Ru_{0.95}O_2^{0.2-}$ and the corresponding height profile. (d) Cross-sectional HRTEM image of the MIM capacitor. (e) EDS analysis of the cross section.

structure of the MIM device. The image confirms the homogeneous film architecture with a total thickness of ~28 nm over a wide range, clearly showing the sandwich structure of $(Ru_{0.95}O_2^{0.2-})_5/(Ca_2Nb_3O_{10}^-)_{10}/(Ru_{0.95}O_2^{0.2-})_5$ (Figure 7d). $Ca_2Nb_3O_{10}^-$ nanosheets stacked in ten layers are resolved, and the distance between neighboring sheets is 1.6 nm, which is in good agreement with XRD results. Each nanosheet layer is imaged as three parallel dark fringes corresponding to a 2D array of apex-sharing NbO_6 octahedra. On the other hand, an expected lamellar feature is not evident for the $Ru_{0.95}O_2^{0.2-}$ nanosheet films, probably due to their thinner and more flexible structure, and also possible beam sensitivity. Their thickness of 5–6 nm is, however, again consistent with that for the five-layer film of this nanosheets. Energy dispersive X-ray spectrometry (EDS) analysis (Figure 7e) was used to probe the compositional distribution across the section of the MIM structure. The profiles of Ru-L and Nb-L (or Ca-K) edge spectra clearly discriminate the electrodes of $Ru_{0.95}O_2^{0.2-}$ and the dielectric layer of $Ca_2Nb_3O_{10}^-$.

One important aspect of the sandwich structure is a clean and sharp interface between $Ru_{0.95}O_2^{0.2-}$ and $Ca_2Nb_3O_{10}^-$ nanosheets. There was no detectable interdiffusion and disorder at the interface, suggesting a good matching between the films of $Ru_{0.95}O_2^{0.2-}$ and $Ca_2Nb_3O_{10}^-$ nanosheets. This sharp interface is an important prerequisite for realizing high performance of the capacitors. The successful construction of the MIM device, which meets such prerequisites, owes to the advantages of the nanosheet assembly processes, which can be conducted at mild and room-temperature conditions.

Electrical Properties of the All-Nanosheet Capacitor. The capacitance density (C) was measured as a function of frequency for the device composed of $(Ru_{0.95}O_2^{0.2-})_2/(Ca_2Nb_3O_{10}^-)_{10}/(Ru_{0.95}O_2^{0.2-})_2$. The results are plotted in Figure 8a. The device shows a stable capacitance density of ~27.5 μF cm^{-2} (~28 nm in thickness) at the high-frequency region from 10 kHz to 1 MHz. The capacitance normalized by the thickness is nearly 10 times that of state-of-the-art HfO_2-based ultrathin capacitors (~0.89 μF cm^{-2}/10 nm)[38] and approximately 2000 times higher than that of commercial capacitors (~20 μF cm^{-2}/5 × 10^4 nm).[39] A parallel-plate capacitor model is generally employed to extract the dielectric response of the capacitor, using the equation $\varepsilon_r = Cd/S\varepsilon_0$, where ε_r denotes the relative permittivity, C is the capacitance, d is the thickness of dielectric layers, S is the area of the capacitor, and ε_0 is vacuum permittivity. The dielectric constant ε_r converted is also shown in Figure 8a. The response may be understood by a universal dielectric relaxation process of dielectric materials. The drop in dielectric constant at low-frequency regions (<1 kHz) implies a finite and reversible storage of charge in $Ca_2Nb_3O_{10}^-$ nanosheet films or at the interface, which is known as low-frequency dispersion (LFD).[40] At high frequencies (1 kHz to 1 MHz), the dielectric performance is nearly constant, showing a gradual but small decline from 150 to 130. This behavior may be described as relatively "shallow"

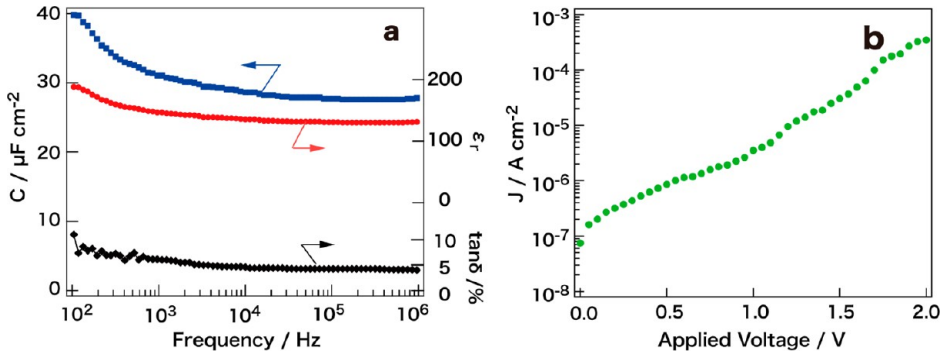

Figure 8. (a) Frequency dependence of dielectric constant ε_r, corresponding capacitance density *C*, and dielectric loss (tan δ). (b) Leakage current *vs* bias voltage (*J*−*V*) profiles of the $(Ru_{0.95}O_2^{0.2-})_2/(Ca_2Nb_3O_{10}^-)_{10}/(Ru_{0.95}O_2^{0.2-})_2$ device.

fractional power laws, which is due to the polarization of dipoles within $Ca_2Nb_3O_{10}^-$ nanosheet films.[40] The observed dielectric constant of 130−150 is much higher than those of other high-*k* materials such as HfO_2 and Ta_2O_5 at a comparable thickness.[38,41−43] On the other hand, the value is somewhat lower than 210 attained for the same dielectric layer in a previous device of Au dot (50 μm ϕ)/$(Ca_2Nb_3O_{10}^-)_{10}$/$SrRuO_3$.[26] In the previous case, the dielectric layer was deposited by the same LB procedure but on a $SrRuO_3$ single-crystal substrate. The atomically flat surface likely leads to a film of more densely packed nanosheets, which may account for the superior dielectric performance. The dielectric loss (tan δ) is also shown in Figure 8a, which gradually decreases from 5.0% to 3.6% when the frequency increases from 1 kHz to 1 MHz.

Leakage current density *vs* bias voltage (*J*−*V*) measurements of the capacitor were conducted by biasing the top electrode of $Ru_{0.95}O_2^{0.2-}$ nanosheets from 0 to 2 V (Figure 8b). The leakage current density is ~3.5 × 10^{-6} A cm^{-2} at a bias voltage of 1.0 V, showing good insulating properties. Nevertheless, this value is to some extent larger when compared with the data (<10^{-7} A cm^{-2}) on the system fabricated on the atomically flat $SrRuO_3$ substrate. This difference may be again related to the substrate effect for dielectric layers; a slightly larger roughness of the $(Ru_{0.95}O_2^{0.2-})_2$ electrodes likely leads to both leakage current and contact resistance effects, which may account for a slightly higher *J* and tan δ, compared to the ideal case of Au dot (50 μm ϕ)/$(Ca_2Nb_3O_{10}^-)_{10}$/$SrRuO_3$.[26] There is a slight inflection point at 0.8 V, suggesting a different carrier transport mechanism working below and above this threshold. The experimental *J*−*V* profiles were fitted based on models involving Schottky emission and Poole−Frenkel effects (see Supporting Information, Figure S6).[43−45] At a low bias voltage (0−0.8 V), the leakage current may pass through the Schottky barrier between $(Ru_{0.95}O_2^{0.2-})_2/(Ca_2Nb_3O_{10}^-)_{10}$, whereas at a high voltage (0.8−2 V), the Poole−Frenkel effect, which is associated with field-enhanced thermal excitation, may dominate the leakage current. For the latter, $Ru_{0.95}O_2^{0.2-}$ electrodes may become a good electron donor under a high electronic field due to surface defects or contaminants. In this regard, fabrication parameters of $Ru_{0.95}O_2^{0.2-}$ electrodes may be further optimized to attain a cleaner and flatter surface. Furthermore, the work function of $Ru_{0.95}O_2^{0.2-}$ may be adjusted by grafting organic molecules on its surface, which is similar to the Au or semiconductor surface.[46] Such a modification may help to further reduce leakage currents.

CONCLUSIONS

In summary, all-nanosheet MIM capacitors have been successfully assembled by the solution-based processes using two types of oxide nanosheets as building blocks. One is $Ru_{0.95}O_2^{0.2-}$ for top and bottom electrodes, and the other is $Ca_2Nb_3O_{10}^-$ for the dielectric layer. The device consists of a sandwich structure of $Ru_{0.95}O_2^{0.2-}/Ca_2Nb_3O_{10}^-/Ru_{0.95}O_2^{0.2-}$ with a total thickness less than 30 nm. The capacitance density is measured to be as high as ~27.5 μF cm^{-2}, which is approximately 2000 times higher than those of currently available commercial products. Thanks to its compatibility with mild solution-based processes at room temperature, there are no strict limitations on the dimensions, shapes, and materials of the substrate, which indicates great advantages when developing large-scale manufacturing processes. The fabrication process involving layer-by-layer assembly of the nanosheets without costly fabrication lines and special annealing processes for metal electrode layers is another big benefit particularly in practical applications for MLCCs. Furthermore, the all-nanosheet capacitors may be readily assembled on plastic or flexible substrates through this approach. The ultrathin all-nanosheet capacitor arrays have the potential to be used as embedded capacitors in printed circuit boards (PCB) and in future high-density dynamic random access memory (DRAM) devices.

We should emphasize that all-nanosheet devices are not specific to material choice and interface geometry; similar interface features and dielectric properties have been observed in the MIM structures with different thickness and/or with other dielectric nanosheets such

as $Ti_{0.87}O_2^{0.52-}$. Also, the virtually infinite varieties of oxide nanosheets, which can be used to assemble various nanosheet architectures, suggest that 2D heterointerfaces will offer an unprecedented versatility for the realization of new 2D states and molecularly thin film devices even beyond graphene.

MATERIALS AND METHODS

Preparation of $Ru_{0.95}O_2^{0.2-}$ and $Ca_2Nb_3O_{10}^-$ Nanosheets. $Ru_{0.95}O_2^{0.2-}$ and $Ca_2Nb_3O_{10}^-$ nanosheets were prepared by delaminating corresponding layered compounds according to procedures reported previously.[28,26] Starting layered compounds of $K_{0.2}RuO_{2.1}\cdot nH_2O$ and $KCa_2Nb_3O_{10}$ were synthesized by a solid-state calcination of a mixture of K_2CO_3/RuO_2 and $K_2CO_3/CaCO_3/Nb_2O_5$ at 850 and 1200 °C, respectively. The obtained samples were subsequently converted into their protonic forms, $H_{0.2}RuO_{2.1}\cdot 0.9H_2O$ and $HCa_2Nb_3O_{10}\cdot 1.5H_2O$, by acid-exchange reaction. These protonated oxides were reacted with aqueous solutions of TBAOH at appropriate concentrations corresponding to equivalent dosing with respect to exchangeable protons in the oxides. The former mixture was shaken vigorously by a mechanical shaker for a week, producing a colloidal suspension with a brownish-black color. The suspension contained unilamellar $Ru_{0.95}O_2^{0.2-}$ nanosheets with an average lateral size of ~1 μm. On the other hand, mild agitation (occasional manual shaking) was applied to the sample of the $HCa_2Nb_3O_{10}\cdot 1.5H_2O$/TBAOH to obtain large-sized nanosheets, given the fact that using such large sheets was essential to attain superior dielectric and insulating performance in a multilayer film form. One-month shaking yielded an opalescent suspension, which contained $Ca_2Nb_3O_{10}^-$ nanosheets with a lateral size of 2–6 μm.

Deposition of $Ru_{0.95}O_2^{0.2-}$ Nanosheet Films as a Bottom Electrode. Colloidal $Ru_{0.95}O_2^{0.2-}$ nanosheets were assembled into multilayer films on a quartz glass substrate through a sequential adsorption process. In a typical process, the substrate was cleaned by treatment with (1:1) CH_3OH/HCl and concentrated H_2SO_4 for 30 min each. The cleaned substrate was primed by immersion in an aqueous solution (1 wt %) of copolymer C-601 (PVAm/PVA = 15 mol %) for 5 min to make its surface positively charged. The resulting substrate was dipped in a diluted suspension of $Ru_{0.95}O_2^{0.2-}$ nanosheets (0.2 g dm^{-3}, no pH adjustment). After 2 min, the substrate was taken out, rinsed meticulously with ultrapure water, and dried under a N_2 gas stream. Deposition of the C-601/$Ru_{0.95}O_2^{0.2-}$ nanosheet bilayer was repeated n times to fabricate a (C-601/$Ru_{0.95}O_2^{0.2-}$)$_n$ film.

Assembly of $Ca_2Nb_3O_{10}^-$ Nanosheet Films as a Dielectric Layer. Multilayer $Ca_2Nb_3O_{10}^-$ nanosheet film was fabricated by the LB method according to procedures previously reported.[31] In a typical process, 0.25 dm^3 of a $Ca_2Nb_3O_{10}^-$ nanosheet suspension (0.032 g dm^{-3}) was gently poured into an LB trough (USI FSD-3-777) equipped with double barriers and a Wilhelmy-type balance for surface pressure measurement. After waiting for 3 min, two barriers were moved inward from both ends of the trough at a rate of 0.25 mm s^{-1} until the surface pressure reached 13 mN m^{-1}. After maintaining a constant pressure for 20 min, the film at the solution/air interface was transferred onto the substrate through the vertical lifting of the substrate immersed in the LB trough at a transfer rate of 1.0 mm min^{-1}. After each LB deposition cycle, the film was dried at 110 °C for 20 min and exposed to UV light from a Xe lamp (1 mW cm^{-2}) for 10 min on either side. The LB process was repeated 10 times to obtain a ten-layer film.

Fabrication of Patterned Films of $Ru_{0.95}O_2^{0.2-}$ Nanosheets as a Top Electrode. An array of circular top electrodes of $Ru_{0.95}O_2^{0.2-}$ nanosheets was fabricated by combined procedures involving photolithography and sequential adsorption. In a typical process, photoresist (AZ-5214E) was deposited on the surface of the ten-layer $Ca_2Nb_3O_{10}^-$ nanosheet films by spin-coating at a speed of 3000 rpm for 60 s. After prebaking at 90 °C for 180 s, the sample covered with the photoresist was exposed to UV light (18 mW cm^{-2}) for 4 s through a photomask. Then a reversal bake at 120 °C for 30 s and a flood exposure of 6 s were carried out. The sample was subsequently developed by NMD-3 for 60 s and rinsed with ultrapure water for 60 s. As a result, hollow columns corresponding to the photomask pattern were formed on the surface of the $Ca_2Nb_3O_{10}^-$ nanosheet film. Next, $Ru_{0.95}O_2^{0.2-}$ nanosheets were assembled onto the film by the sequential adsorption process mentioned above. The sample was then immersed into Remover PG for more than 3 h to remove the remaining photoresist and rinsed with isopropyl alcohol and ultrapure water twice. Finally, the sample was exposed to UV light for 24 h to completely decompose organic moieties in the nanosheet galleries.

Characterization. XRD data were collected by a Rigaku RINT 2200 powder diffractometer with monochromatized Cu Kα radiation (λ = 0.15405 nm). UV–visible absorption spectra were recorded on a Hitachi U-4100 spectrophotometer. An SII Nanotechnology AFM was employed to examine the surface topography of the nanosheet films. Cross-sectional HRTEM images were taken using a Hitachi H-9000 microscope operating at 200 kV. An Olympus BX 51-P optical microscope and Keyence VE-8800 SEM were employed to observe the surface textures of samples, particularly the patterned circular films of $Ru_{0.95}O_2^{0.2-}$ nanosheets. Sheet resistances of $Ru_{0.95}O_2^{0.2-}$ nanosheets were characterized using films with Au electrodes. Au contacts were evaporated over the film through a metal mask. Sheet resistance was measured using a semiconductor parameter analyzer (Keithley 4200-SCS). Leakage currents and dielectric properties of the ultrathin capacitors were measured using a dielectric test system consisting of a semiconductor parameter analyzer (Keithley 4200-SCS) and a precision impedance analyzer (Agilent Technologies 4294A).

Conflict of Interest: The authors declare no competing financial interest.

Acknowledgment. This research was supported by CREST of the Japan Science and Technology Agency (JST) and the World Premier International Research Center (WPI) Initiative on Materials Nanoarchitectonics, MEXT, Japan. We thank Dr. Q. Wang and Mr. A. Ohi at MANA for the discussion and help with the photolithography process.

Supporting Information Available: AFM images of monolayer and two- and five-layer films of $Ru_{0.95}O_2^{0.2-}$ nanosheets and monolayer and ten-layer films of $Ca_2Nb_3O_{10}^-$ nanosheets, UV–visible absorption spectra of the $Ru_{0.95}O_2^{0.2-}$ and $Ca_2Nb_3O_{10}^-$ nanosheet films before and after the photolithography process, optical microscopy photographs of the top of the capacitors, and analysis of the mechanism of leakage current. This material is available free of charge via the Internet at http://pubs.acs.org.

REFERENCES AND NOTES

1. van Dover, R. B.; Schneemeyer, L. F.; Fleming, R. M. Discovery of a Useful Thin-Film Dielectric Using a Composition-Spread Approach. *Nature* **1998**, *392*, 162–164.
2. Jillek, W.; Yung, W. K. C. Embedded Components in Printed Circuit Boards: A Processing Technology Review. *Int. J. Adv. Manuf. Technol.* **2005**, *25*, 350–360.
3. Randall, C. A. Scientific and Engineering Issues of the State-of-the-Art and Future Multilayer Capacitors. *J. Ceram. Soc. Jpn.* **2001**, *109*, S2–S6.
4. Kishi, H.; Mizuno, Y.; Chazono, H. Base-Metal Electrode-Multilayer Ceramic Capacitors: Past, Present and Future Perspectives. *Jpn. J. Appl. Phys.* **2003**, *42*, 1–15.
5. Pithan, C.; Hennings, D.; Waser, R. Progress in the Synthesis of Nanocrystalline $BaTiO_3$ Powders for MLCC. *Int. J. Appl. Ceram. Technol.* **2005**, *2*, 1–14.
6. http://www.murata.com/products/capacitor/design/data/property.html.

7. Krupanidhi, S. B.; Peng, C.-J. Studies on Structural and Electrical Properties of Barium Strontium Titanate Thin Films Developed by Metallo-Organic Decomposition. *Thin Solid Films* **1997**, *305*, 144–156.
8. Niinistö, J.; Kukli, K.; Heikkilä, M.; Ritala, M.; Leskelä, M. Atomic Layer Deposition of High-*k* Oxides of the Group 4 Metals for Memory Applications. *Adv. Eng. Mater.* **2009**, *11*, 223–234.
9. No, S. Y.; Oh, J. H.; Jeon, C. B.; Schindler, M.; Hwang, C. S.; Kim, H. J. Study on the Step Coverage of Metallorganic Chemical Vapor Deposited TiO_2 and $SrTiO_3$ Thin Films. *J. Electrochem. Soc.* **2005**, *152*, C435–C441.
10. Baumert, B. A.; Chang, L.-H.; Matsuda, A. T.; Tsai, T.-L.; Tracy, C. J.; Gregory, R. B.; Fejes, P. L.; Cave, N. G.; Chen, W.; Taylor, D. J.; *et al*. Characterization of Sputtered Barium Strontium Titanate and Strontium Titanate-Thin Films. *J. Appl. Phys.* **1997**, *82*, 2558–2566.
11. Thielsch, R.; Kaemmer, K.; Holzapfel, B.; Schultz, L. Structure-Related Optical Properties of Laser-Deposited $Ba_xSr_{1-x}TiO_3$ Thin Films Grown on MgO (001) Substrates. *Thin Solid Films* **1997**, *301*, 203–210.
12. Choy, K. L. Chemical Vapour Deposition of Coatings. *Prog. Mater. Sci.* **2003**, *48*, 57–170.
13. Pulver, M.; Nemetz, W.; Wahl, G. CVD of ZrO_2, Al_2O_3 and Y_2O_3 from Metalorganic Compounds in Different Reactors. *Surf. Coat. Technol.* **2000**, *125*, 400–406.
14. Cho, H. J.; Kim, Y. D.; Park, D. S.; Lee, E.; Park, C. H.; Jang, J. S.; Lee, K. B.; Kim, H. W.; Ki, Y. J.; Han, I. K.; *et al*. New TIT Capacitor with $ZrO_2/Al_2O_3/ZrO_2$ Dielectrics for 60 nm and below DRAMs. *Solid-State Electron.* **2007**, *51*, 1529–1533.
15. Cheng, Y.-L.; Hsieh, C.-Y.; Chang, Y.-L. Deposition Cycle of Atomic Layer Deposition HfO_2 Film: Effects on Electrical Performance and Reliability. *Thin Solid Films* **2013**, *528*, 77–81.
16. Weinreich, W.; Wilde, L.; Müller, J.; Sundqvist, J.; Erben, E.; Heitmann, J.; Lemberger, M.; Bauer, A. J. Structural Properties of as Deposited and Annealed ZrO_2 Influenced by Atomic Layer Deposition, Substrate, and Doping. *J. Vac. Sci. Technol. A* **2013**, *31*, 01A119.
17. Perkins, C. M.; Triplett, B. B.; McIntyre, P. C.; Saraswat, K. C.; Shero, E. Thermal Stability of Polycrystalline Silicon Electrodes on ZrO_2 Gate Dielectrics. *Appl. Phys. Lett.* **2002**, *81*, 1417–1419.
18. Gallegos, J. J.; Ward, T. L.; Boyle, T. J.; Rodriguez, M. A.; Francisco, L. P. Neo-Pentoxide Precursors for MOCVD Thin Films of TiO_2 and ZrO_2. *Chem. Vap. Deposition* **2000**, *6*, 21–26.
19. Battiston, G. A.; Gerbasi, R.; Porchia, M. Influence of Substrate on Structural Properties of TiO_2 Thin Films Obtained *via* MOCVD. *Thin Solid Films* **1994**, *239*, 186–191.
20. Babelon, P.; Dequiedt, A. S.; Mostéfa-Sba, H.; Bourgeois, S.; Sibillot, P.; Sacilotti, M. SEM and XPS Studies of Titanium Dioxide Thin Films Grown by MOCVD. *Thin Solid Films* **1998**, *322*, 63–67.
21. Nasir, S.; Saleemi, A. S.; Fatima-tuz-Zahra; Anis-ur-Rehman, M. Enhancement in Dielectric and Magnetic Properties of Ni-Zn Ferrites Prepared by Sol−Gel Method. *J. Alloys Compd.* **2013**, *572*, 170–174.
22. Hwang, C. S.; Park, S. O.; Cho, H.-J.; Kang, C. S.; Kang, H.-K.; Lee, S. I.; Lee, M. Y. Deposition of Extremely Thin $(Ba,Sr)TiO_3$ Thin Films for Ultra-Large-Scale Integrated Dynamic Random Access Memory Application. *Appl. Phys. Lett.* **1995**, *67*, 2819–2821.
23. Chang, W.; Gilmore, C. M.; Kim, W.-J.; Pond, J. M.; Kirchoefer, S. W.; Qadri, S. B.; Chirsey, D. B.; Horwitz, J. S. Influence of Strain on Microwave Dielectric Properties of $(Ba,Sr)TiO_3$ Thin Films. *J. Appl. Phys.* **2000**, *87*, 3044–3049.
24. Park, B. H.; Peterson, E. J.; Jia, Q. X.; Lee, J.; Zeng, X.; Si, W.; Xi, X. X. Effects of Very Thin Strain Layers on Dielectric Properties of Epitaxial $Ba_{0.6}Sr_{0.4}TiO_3$ Films. *Appl. Phys. Lett.* **2001**, *78*, 533–535.
25. Osada, M.; Ebina, Y.; Funakubo, H.; Yokoyama, S.; Kiguchi, T.; Takada, K.; Sasaki, T. High-*k* Dielectric Nanofilms Fabricated from Titania Nanosheets. *Adv. Mater.* **2006**, *18*, 1023–1027.
26. Osada, M.; Akatsuka, K.; Ebina, Y.; Funakubo, H.; Ono, K.; Takada, K.; Sasaki, T. Robust High-*k* Response in Molecularly Thin Perovskite Nanosheets. *ACS Nano* **2010**, *4*, 5225–5232.
27. Osada, M.; Takanashi, G.; Li, B.-W.; Akatsuka, K.; Ebina, Y.; Ono, K.; Funakubo, H.; Takada, K.; Sasaki, T. Controlled Polarizability of One-Nanometer-Thick Oxide Nanosheets for Tailored, High-*k* Nanodielectrics. *Adv. Funct. Mater.* **2011**, *21*, 3482–3487.
28. Sato, J.; Kato, H.; Kimura, M.; Fukuda, K.; Sugimoto, W. Conductivity of Ruthenate Nanosheets Prepared *via* Electrostatic Self-Assembly: Characterization of Isolated Single Nanosheet Crystallite to Mono- and Multilayer Electrodes. *Langmuir* **2010**, *26*, 18049–18054.
29. Fukuda, K.; Saida, T.; Sato, J.; Yonezawa, M.; Takasu, Y.; Sugimoto, W. Synthesis of Nanosheet Crystallites of Ruthenate with an α-$NaFeO_2$-Related Structure and Its Electrochemical Supercapacitor Property. *Inorg. Chem.* **2010**, *49*, 4391–4393.
30. Osada, M.; Sasaki, T. Two-Dimensional Dielectric Nanosheets: Novel Nanoelectronics from Nanocrystal Building Blocks. *Adv. Mater.* **2012**, *24*, 210–228.
31. Li, B.-W.; Osada, M.; Ozawa, T. C.; Ebina, Y.; Akatsuka, K.; Ma, R.; Funakubo, H.; Sasaki, T. Engineered Interfaces of Artificial Perovskite Oxide Superlattices *via* Nanosheet Deposition Process. *ACS Nano* **2010**, *4*, 6673–6680.
32. Kawahara, T.; Yamamuka, M.; Yuuki, A.; Ono, K. $(Ba, Sr)TiO_3$ Films Prepared by Liquid Source Chemical Vapor Deposition on Ru Electrodes. *Jpn. J. Appl. Phys.* **1996**, *35*, 4880–4885.
33. Huang, A.; Shannigrahi, S. R. Effect of Bottom Electrode and Resistive Layer on the Dielectric and Ferroelectric Properties of Sol-Gel Derived $BiFeO_3$ Thin Films. *J. Alloys Compd.* **2011**, *509*, 2054–2059.
34. Fröhlich, K.; Aarik, J.; Ťapajna, M.; Rosová, A.; Aidla, A.; Dobročka, E.; Hušková, K. Epitaxial Growth of High-*k* TiO_2 Rutile Films on RuO_2 Electrodes. *J. Vac. Sci. Technol. B* **2009**, *27*, 266–270.
35. Zhong, H.; Heuss, G.; Misra, V.; Luan, H.; Lee, C.-H.; Kwong, D.-L. Characterization of RuO_2 Electrodes on Zr Silicate and ZrO_2 Dielectrics. *Appl. Phys. Lett.* **2001**, *78*, 1134–1136.
36. Akatsuka, K.; Haga, M.; Ebina, Y.; Osada, M.; Fukuda, K.; Sasaki, T. Construction of Highly Ordered Lamellar Nanostructures through Langmuir-Blodgett Deposition of Molecularly Thin Titania Nanosheets Tens of Micrometers Wide and Their Excellent Dielectric Properties. *ACS Nano* **2009**, *3*, 1097–1106.
37. Sasaki, T.; Ebina, Y.; Fukuda, K.; Tanaka, T.; Harada, M.; Watanabe, M. Titania Nanostructured Films Derived from a Titania Nanosheet/Polycation Multilayer Assembly *via* Heat Treatment and UV Irradiation. *Chem. Mater.* **2002**, *14*, 3524–3530.
38. Sangwan, V. K.; Jariwala, D.; Filippone, S. A.; Karmel, H. J.; Johns, J. E.; Alaboson, J. M. P.; Marks, T. J.; Lauhon, L. J.; Hersam, M. C. Quantitatively Enhanced Reliability and Uniformity of High-*k* Dielectrics on Graphene Enabled by Self-Assembled Seeding Layers. *Nano Lett.* **2013**, *13*, 1162–1167.
39. http://www.murata.com/new/news_release/2009/1005b/index.html.
40. Jonscher, A. K. Dielectric Relaxation in Solids. *J. Phys. D: Appl. Phys.* **1999**, *32*, R57–R70.
41. Lee, B. H.; Kang, L.; Nieh, R.; Qi, W.-J.; Lee, J. C. Thermal Stability and Electrical Characteristics of Ultrathin Hafnium Oxide Gate Dielectric Reoxidized with Rapid Thermal Annealing. *Appl. Phys. Lett.* **2000**, *76*, 1926–1928.
42. Zhao, X.; Vanderbilt, D. First-Principles Study of Structural, Vibrational, and Lattice Dielectric Properties of Hafnium Oxide. *Phys. Rev. B* **2002**, *65*, 233106.
43. Chaneliere, C.; Autran, J. L.; Devine, R. A. B.; Balland, B. Tantalum Pentoxide (Ta_2O_5) Thin Films for Advanced Dielectric Applications. *Mater. Sci. Eng., R* **1998**, *22*, 269–322.
44. Emtage, P. R.; Tantraporn, W. Schottky Emission through Thin Insulating Films. *Phys. Rev. Lett.* **1962**, *8*, 267–268.
45. Simmons, J. G. Poole-Frenkel Effect and Schottky Effect in Metal-Insulator-Metal Systems. *Phys. Rev.* **1967**, *155*, 657–660.
46. Ashkenasy, G.; Cahen, D.; Cohen, R.; Shanzer, A.; Vilan, A. Molecular Engineering of Semiconductor Surfaces and Devices. *Acc. Chem. Res.* **2002**, *35*, 121–128.